25th ABCM International Congress of Mechanical Engineering
October 20-25, 2019, Uberlândia, MG, Brazil

COB-2019-1247
NUMERICAL AND EXPERIMENTAL STUDY OF GAS-LIQUID FLOWS IN A CENTRIFUGAL ROTOR

Henrique Stel
Edgar M. Ofuchi
Jhoan M. C. Cubas
Rafael F. Alves
Rigoberto E. M. Morales
Federal University of Technology – Paraná – UTFPR, Multiphase Flow Research Center – NUEM.
Rua Dep. Heitor Alencar Furtado 5000, Curitiba, 81280340, Brazil
edgarofuchi@gmail.com
stel.henrique@gmail.com
jhoancbs2@gmail.com
rafabricio@live.com
rmorales@utfpr.edu.br

Abstract. *This work presents a numerical and experimental study of gas-liquid flows in a centrifugal rotor. The numerical model is based on the Two-Fluid Model and a polydispersed approach, accounting for the effect of several two-phase flow interactions, including bubble breakup and coalescence. The model is compared with an experimental loop designed to evaluate pressure rise curves and flow pattern visualization in the centrifugal rotor. Association of images from the experiments with the behavior of the pressure rise curves reveal the existence of several, well distinct two-phase flow patterns that significantly affect the performance of the centrifugal rotor. Comparison of numerical results with the experimental data yield good agreement for both performance parameters and flow patterns. In particular, the numerical model is able to capture the abrupt drop of the pressure rise curve associated with the formation of gas pockets in the rotor channels, as well as the bubble size distribution resulted from the bubble breakup and coalescence interactions. Outcomes from this work could help further understanding of the complex gas-liquid flow behavior inside turbomachines, a topic that is of interest in important industrial processes such as safety of nuclear plants and petroleum production.*

Keywords: *numerical simulation, experimental, gas-liquid flows, centrifugal pump.*

1. INTRODUCTION

Centrifugal pumps operating with gas-liquid flows constitute an off-design condition associated with unstable behavior and performance degradation. Industrial processes where this can be a concern include loss-of-coolant accidents in nuclear reactors and in petroleum production.

Although pumps are able to handle gas-liquid flows, the presence of a secondary gas phase can induce additional hydraulic losses that impair the ability of the pump to deliver proper head and flow rate. In particular, there is a tendency of the gas phase to be accumulate in the pump impellers in the form of gas pockets, which leads to unstable operation and causes an abrupt drop in performance. Informally, this is called as “surging” in the petroleum industry (Gamboa, 2008).

Investigations through the past decades revealed that the surging event, as well as the range for which the performance degradation under gas-liquid pumping is tolerable, are dependent on several parameters, such as the liquid and gas flow rates, the impeller rotating speed, the gas density and the pump geometry. Effort to investigate the effect of many parameters on the pump performance can be found on numerous experimental investigations.

Few investigations, however, bring together flow visualization to understand the physics behind the behavior of centrifugal pumps with gas-liquid flows. Works such as Murakami and Minemura (1974) and Gamboa (2008) were able to visualize flow patterns in impeller prototypes or modified pump stages. These works provide great global insight on the phenomenon, revealing that, as with pipe flows, gas-liquid flows in pumps are also subject to distinct flow patterns. One issue is that pumps involve rotating parts and limited visual access, sometimes making it hard to interpret flow patterns and to understand complex phenomena, such as bubble breakup and coalescence.

Computational fluid dynamics could help assessing many details of two-phase flows in pumps. However, numerical studies about the subject are rare in literature. Works employing eulerian methods for qualitative analysis of gas-liquid

flows in impellers are proposed by Caridad and Kenyery (2004) and a few others. Besides many geometric simplifications adopted in most works, the gas phase is usually modeled as monodispersed, and several important gas-liquid interactions are disregarded, such as bubble breakup and coalescence. Validation against experimental data in similar conditions is hardly found.

Following the above context, this article presents a numerical and experimental work to study gas-liquid flows in a centrifugal rotor. An Euler-Euler polydispersed numerical approach is used to calculate performance curves and to understand the flow pattern inside the rotor. Boundary conditions and data for validation are obtained with a novel experimental setup designed to overcome many disadvantages of previous investigations. Combining both procedures helps in the direction of validating a numerical model for reliable simulations of gas-liquid flows in pumps, which is lacking in the current literature.

2. NUMERICAL APPROACH

An Euler-Euler approach (Yeoh and Tu, 2009) is proposed to model air-water flows inside a centrifugal rotor. The mass and momentum conservation equations are described in Eq. (1) and (2)

$$\frac{\partial \alpha_i \rho_i^X}{\partial t}^{(i)} + \nabla \cdot \left(\alpha_i \rho_i^X \vec{V}_i^{X\rho} \right)^{(ii)} = \Gamma_i^{(iii)} \tag{1}$$

$$\frac{\partial \alpha_i \rho_i^X \vec{V}_i^{X\rho}}{\partial t}^{(iv)} + \nabla \cdot \left(\alpha_i \rho_i^X \vec{V}_i^{X\rho} \vec{V}_i^{X\rho} \right)^{(v)} = -\nabla \left(\alpha_i p_i^X \right)^{(vi)} + \alpha_i \left(\mu_i^X + \mu_{i,t}^X \right)^{(vii)} \cdot \nabla^2 \vec{V}_i^{X\rho} + \\ + \alpha_i \rho_i^X \vec{g}^{X\rho}{}^{(viii)} - \alpha_i \rho_i^X \left(\vec{\Omega}^{X\rho} \times \vec{V}_i^{X\rho} \right)^{(ix)} - \alpha_i \rho_i^X \vec{\Omega}^{X\rho} \times \left(\vec{\Omega}^{X\rho} \times \vec{r}^{X\rho} \right)^{(x)} + \vec{M}_i^{(xi)} + \vec{V}_i^m \Gamma_i^{(xii)} \tag{2}$$

In Eq. (1), the terms (*i*), (*ii*) and (*iii*) are the mass variation in the control volume, the mass flux through the control volume surfaces and the interfacial mass exchange, respectively. Each term is weighted by the phase volume fraction α_i. Terms (*iv*) and (*v*) in Eq. (2) are the advective and temporal accelerations. While, terms (*vi*), (*vii*), (*viii*), (*ix*), (*x*), (*xi*) and (*xii*) are, respectively, the pressure gradient, the viscous tensor that englobes laminar and turbulent effects, the gravitational force, the Coriolis force, the centrifugal force, the interfacial momentum transfer, and momentum exchange due to mass transfer at the interface. The superscript X and $X\rho$ in Eq. (2) indicates that a phase average or a Favre average is used.

In the present work, there is no mass transfer between the phases. Thus, terms, (*iii*) from Eq. (1) and (*xii*) from Eq. (2) are neglected. The term that englobes the interfacial momentum transfer (*xi*) is considered in Eq. (3), where the term is separated by several forces (drag, virtual mass, lift, wall lubrication and turbulent dispersion forces), described below.

$$\vec{M}_i = \alpha_k \frac{\vec{F}_D + \vec{F}_{VM} + \vec{F}_L + \vec{F}_{WL} + \vec{F}_{TD}}{\forall_p} \tag{3}$$

The drag force ($\vec{F}_D$) acts against the main movement. Considering a spherical bubble with diameter d_b, the drag force is calculated by:

$$\vec{F}_{D,LG} = -\frac{1}{2} C_D \cdot \rho_L \cdot \left(\vec{V}_G - \vec{V}_L \right) \cdot \left| \vec{V}_G - \vec{V}_L \right| \cdot \frac{\pi d_b^2}{4} \tag{4}$$

where, C_D is the drag coefficient and depends on the geometrical shape of the bubble and the gas volume fraction. Eq. (5) is used to calculate the C_D, while Eqs. (6) and (7) are used to determine the drag coefficient for spherical, ellipsoid and cap bubble geometries.

$$C_D = \left(1 - \alpha_G\right)^{-0.5} \cdot \max\left(C_{D,sph}; C_{D,dist} \right) \tag{5}$$

Equation (6) models the $C_{D,sph}$, in which it is the C_D for spherical regime and depends on the particle Reynolds number, Re_p.

$$C_{D,sph} = \max\left[\frac{24}{Re_p}\left(1+0.15Re_p^{0.687}\right);0.44\right]$$
$$Re_p = \frac{\rho_L \cdot \left|\vec{V}_G - \vec{V}_L\right| \cdot d_b}{\mu_L} \tag{6}$$

The $C_{D,dist}$ (Eq. 5) accounts for the cap bubbles, in which $C_{D,cap} = 8/3$, and for ellipsoid bubbles. The $C_{D,ellip}$ depends on the terminal velocity, U_T, Morton number, Mo, and Eotvos number, Eo, and is modeled by Eq. (7).

$$C_{D,dist} = \min\left(C_{D,ellip}, C_{D,cap}\right)$$
$$C_{D,ellip} = \frac{4}{3}\frac{gd_b}{U_T^2}\frac{\left(\rho_L - \rho_G\right)}{\rho_L}, \text{ where}$$
$$U_T = \frac{\mu_L}{\rho_L d_b} Mo^{-0.149}\left(J - 0.857\right);\ Mo = \frac{g\mu_L^4\left(\rho_L - \rho_G\right)}{\rho_L^2\sigma^3} \tag{7}$$
$$J = \begin{cases} 0.94G^{0.757} & 2 < G \le 59.3 \\ 3.42G^{0.441} & G > 59.3 \end{cases},\ G = \frac{4}{3}EoMo^{-0.149}\left(\frac{\mu_L}{0.0009}\right);\ Eo = \frac{\left(\rho_L - \rho_G\right)gd_b^2}{\sigma}$$

Equation (8) is used to model the virtual mass force, which is the necessary force to push a liquid mass ahead of him. It is based on the liquid mass $C_{VM} \cdot m_L$, and the accelerations of the liquid and gas phases. The liquid mass displaced is $m_L = \rho_L \pi d_b^3 / 6$ and $C_{VM} = 0.5$ is generally assumed.

$$\vec{F}_{VM} = -C_{VM} \cdot m_L \cdot \left(\frac{D_G\vec{V}_G}{Dt} - \frac{D_L\vec{V}_L}{Dt} + 2\vec{\Omega}\times\left(\vec{V}_G - \vec{V}_L\right)\right) \tag{8}$$

The lift force occurs when the bubble is in an asymmetric velocity field and is displaced laterally. The liquid velocity difference acting on the bubble rotates it, which creates a local acceleration. The lift force is expressed by Eq. (9).

$$\vec{F}_L = -C_L \cdot \rho_L \cdot \frac{\pi d_b^3}{6} \cdot \left[\left(\vec{V}_G - \vec{V}_L\right) \times rot(\vec{V}_L)\right] \tag{9}$$

where, C_L is calculated based on the Tomiyama (1988) model, given by Eq. (10).

$$C_L = \begin{cases} min\left(0.288\tanh\left(0.121Re_p\right); f\left(Eo'\right)\right) & Eo' \le 4 \\ f\left(Eo'\right) & 4 < Eo' \le 10 \\ -0.27 & 10 < Eo' \end{cases},$$
$$f\left(Eo'\right) = 0.00105\left(Eo'\right)^3 - 0.0159\left(Eo'\right)^2 - 0.0204Eo' + 0,474, \tag{10}$$
$$Eo' = \frac{g\left(\rho_L - \rho_G\right)d_{b,def}^2}{\sigma};\ d_{b,def} = d_b\left(1 + 0{,}163Eo^{0{,}757}\right)^{1/3}$$

The wall lubrication force occurs when the bubbles are near the walls. This force acts on the bubbles pushing them away from the wall. This force is modelled by Eq. (11) which is from the work of Antal et al. (1991).

$$\vec{F}_{WL} = -C_{WL}\frac{\rho_L\left|\left(\vec{V}_G - \vec{V}_L\right) - \left[\vec{n}_w \cdot \left(\vec{V}_G - \vec{V}_L\right)\right]\vec{n}_w\right|^2}{2}\left(\frac{\pi d_b^2}{4}\right)\vec{n}_w;\ C_{WL} = \max\left(0; -\frac{0.01}{d_b} + \frac{0.05}{\delta_w}\right) \tag{11}$$

The turbulent dispersion force acts on bubble agglomeration dispersing peaks of high concentration. This term arise from the Favre average in the drag force and is modelled by Eq. (12).

$$\vec{M}_{TD} = -\frac{3}{4} C_{TD} C_D \frac{\alpha_G}{d_b} \left|\vec{V}_G - \vec{V}_L\right| \frac{\mu_{L,t}}{\sigma_{TD}} \cdot \left(\frac{1}{\alpha_L} + \frac{1}{\alpha_G}\right) \nabla \alpha_G \tag{12}$$

The input of gas in a liquid flow causes an effect on the turbulence of the liquid phase. Sato and Sekoguchi (1975) modelled this effect using an apparent viscosity, $\mu_{t,app}$, in which the turbulence caused by the bubbles is added into the single phase turbulence, that is:

$$\begin{aligned} \mu_{t,ap} &= \mu_t + \mu_{t,ib} \\ \mu_{t,ib} &= \kappa_{Sato} \rho_L d_b \alpha_G \left|\vec{V}_G - \vec{V}_L\right| \end{aligned} \tag{13}$$

where, $\mu_{t,ib}$ is the turbulence caused by the presence of the bubbles, which depends on the liquid density, ρ_L, the bubble diameter, d_b, the local gas volume fraction, α_G, and a coefficient, κ_{Sato}, assumed as 0.6 in this work.

Many numerical works on two-phase dispersed flows considers a mean diameter. This conservative form of evaluate the problem may deviate from real applications. In addition, bubble interactions, like breakup or coalescence are not considered in a mean diameter approach. To solve this problem the Multiple Size Group (MUSIG – Lo,1996) is used in this work. It is based on a population balance theory, in which a finite number of dimensional groups occur in the flow. The model is coupled in the two-fluid model through the size fraction occupied by a given group in a given volume, $f_m = N_m / \alpha_i$, from which a transport equation (Eq. 13) is derived

$$\frac{\partial \alpha_i \rho_i^X f_m}{\partial t}^{(i)} + \nabla \cdot \left(\alpha_i \rho_i^X \vec{V}_i^{X\rho} f_m\right)^{(ii)} = B_m^{c(iii)} - D_m^{c(iv)} + B_m^{b(v)} - D_m^{b(vi)} \tag{14}$$

The terms on the left hand side of Eq. (13) represents the size fraction, f_m, growth rate in a given volume (*i*) and the flux of f_m through the volume (*ii*). The terms (*iii*) and (*iv*) represents the birth and death rates of a given *m* group due to coalescence, while terms (*v*) and (*vi*) are the birth and death rates due to breakup. The death and birth rates are modeled through breakup and coalescence models, which is described below.

The breakup is modeled by Eq. (12) from the work of Luo and Svendsen (1996). It is a kernel function, $Q(m_m; m_n)$, which describes the breakup rate of a *m* group with mass m_m to a *n* group with mass m_n.

$$Q(m_m; m_n) = 0{,}923 C_Q \left(1 - \alpha_G\right) \left(\frac{\varepsilon_L}{d_{b,m}^2}\right)^{1/3} \int_{\xi_{\min}}^{1} \frac{(1+\xi)^2}{\xi^{11/3}} e^{-\chi} d\xi \tag{15}$$

C_Q is the breakup coefficient, α_g is the local gas volume fraction, $d_{b,m}$ is the *m* group bubble size, ε_L is the turbulent Kinect energy dissipation rate, ξ is a dimensionless length, $\xi = l / d_{b,m}$, in which *l* is the turbulent length scale and χ is a function modeled by Eq. (15).

$$\chi = \frac{6\left[\left(m_n / m_m\right)^{2/3} + \left(1 - m_n / m_m\right)^{2/3} - 1\right]\sigma}{\rho_L \varepsilon_L^{2/3} d_{b,m}^{5/3} \xi^{11/3}} \tag{16}$$

The coalescence model is based on the work of Prince and Blanch (1990) and only the coalescence due to turbulence is considered in this work. The coalescence model is also based on a kernel function, given by Eq. (16).

$$C(m_m; m_n) = \Theta_{mn}^{Turb} \eta_{mn} \tag{17}$$

Eq. (16) accounts the shocks between the bubbles due to turbulence, Θ_{mn}^{Turb}, and a coalescence efficiency, η_{mn}. Eq. (17) models the turbulent bubble collisions, which depends on ε_L, the bubbles diameters, $d_{b,m}$ and $d_{b,n}$, and a coalescence coefficient $C_{L,turb}$ in which a default value of 1 is assumed.

$$\Theta_{mn}^{Turb} = C_{C,turb} \cdot 0.089 \pi \varepsilon_L^{1/3} \left(d_{b,m} + d_{b,n}\right)^2 \left(d_{b,m}^{2/3} + d_{b,n}^{2/3}\right)^{1/2} \tag{18}$$

The coalescence efficiency is modeled thorough Eq. (18) and it is the ratio between the time required to drain the liquid film between the bubbles and the time in which the bubbles stay in contact.

$$\eta_{mn} = e^{-\left(\ln(h_0/h_f)\cdot\left(\rho_L r_{mn}^3/(16\sigma)\right)^{0,5}\right)/\left(r_{mn}^{2/3}/\varepsilon_L^{1/3}\right)} \tag{19}$$

h_0 and h_f are the initial and critical liquid films and r_{mn} is the equivalent radius of the bubble pair group m-n, that is calculated as $r_{mn} = 0,25\cdot(1/d_{b,m} + 1/d_{b,n})^{-1}$. For air-water system, it is assumed $h_0 = 1\times10^{-4}$ m and $h_f = 1\times10^{-8}$ m.

Numerically, the problem is solved following the Element based Finite Volume Method as implemented in ANSYS ® CFX ®. A multi-block technique is used to model this problem, which each component is considered as a sub-domain with its own mesh and reference frame. The sub-domains are connected by an interface algorithm that allows mesh dislocation between them. Figure 1 shows the hexahedral mesh used in this investigation. Setups such as the bubble size range implemented in the MUSIG model and boundary conditions are obtained from an experimental facility designed for this investigation, which is discussed below.

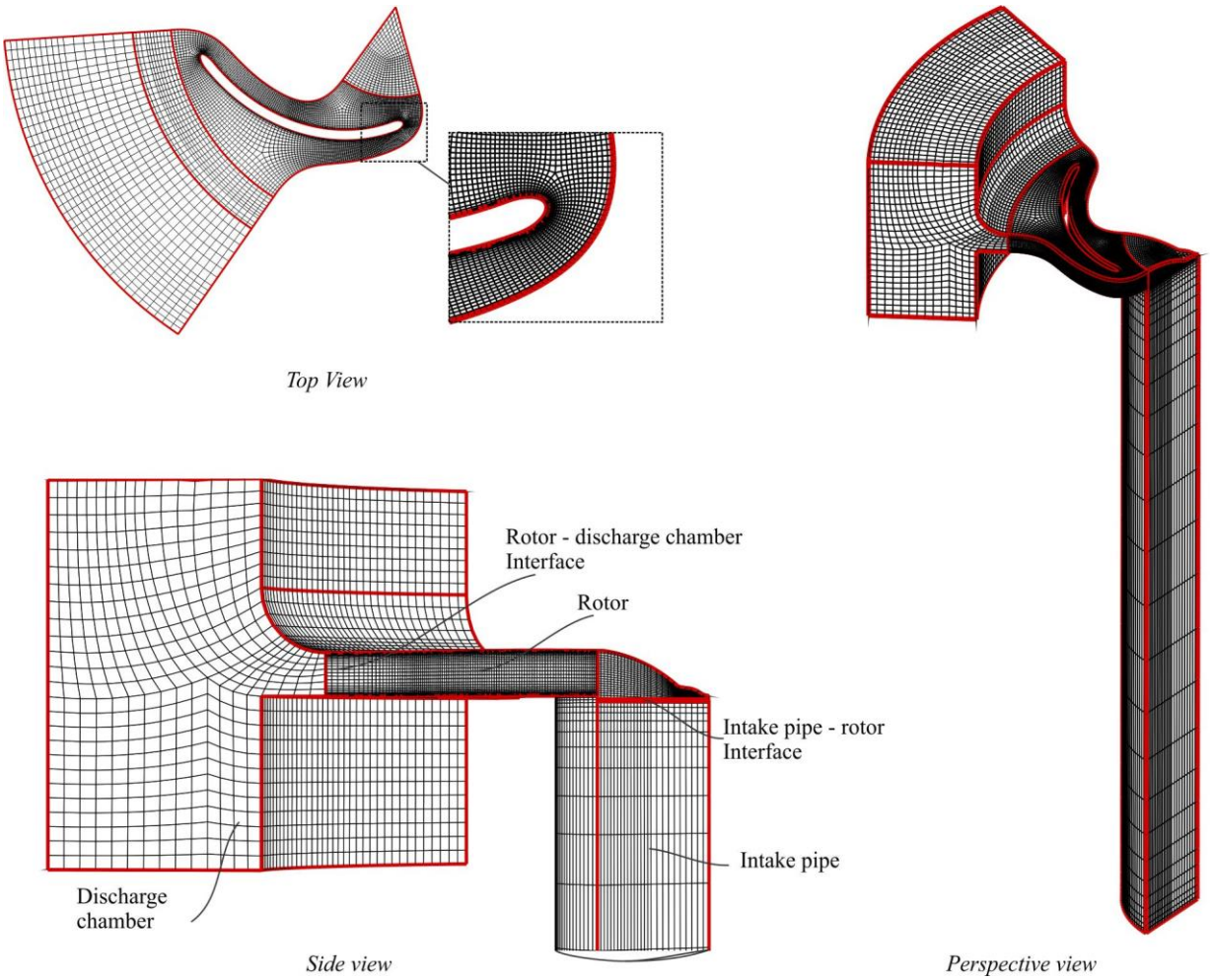

Figure 1. Views of the numerical mesh.

3. EXPERIMENTAL FACILITY

Figure 2 presents a scheme of the experimental loop and the test section used to study gas-liquid flows in a centrifugal rotor under several operating conditions. The experimental loop is composed by a liquid and gas lines that are mixture in the vertical intake pipe before entering the rotor. The liquid-gas mixture is collected in the discharge chamber and returns to the water tank where it is separated. The test section is composed of a vertical intake pipe, a radial rotor and a discharge chamber. The rotor is driven by an electric motor, the speed of which is controlled by a variable-speed drive.

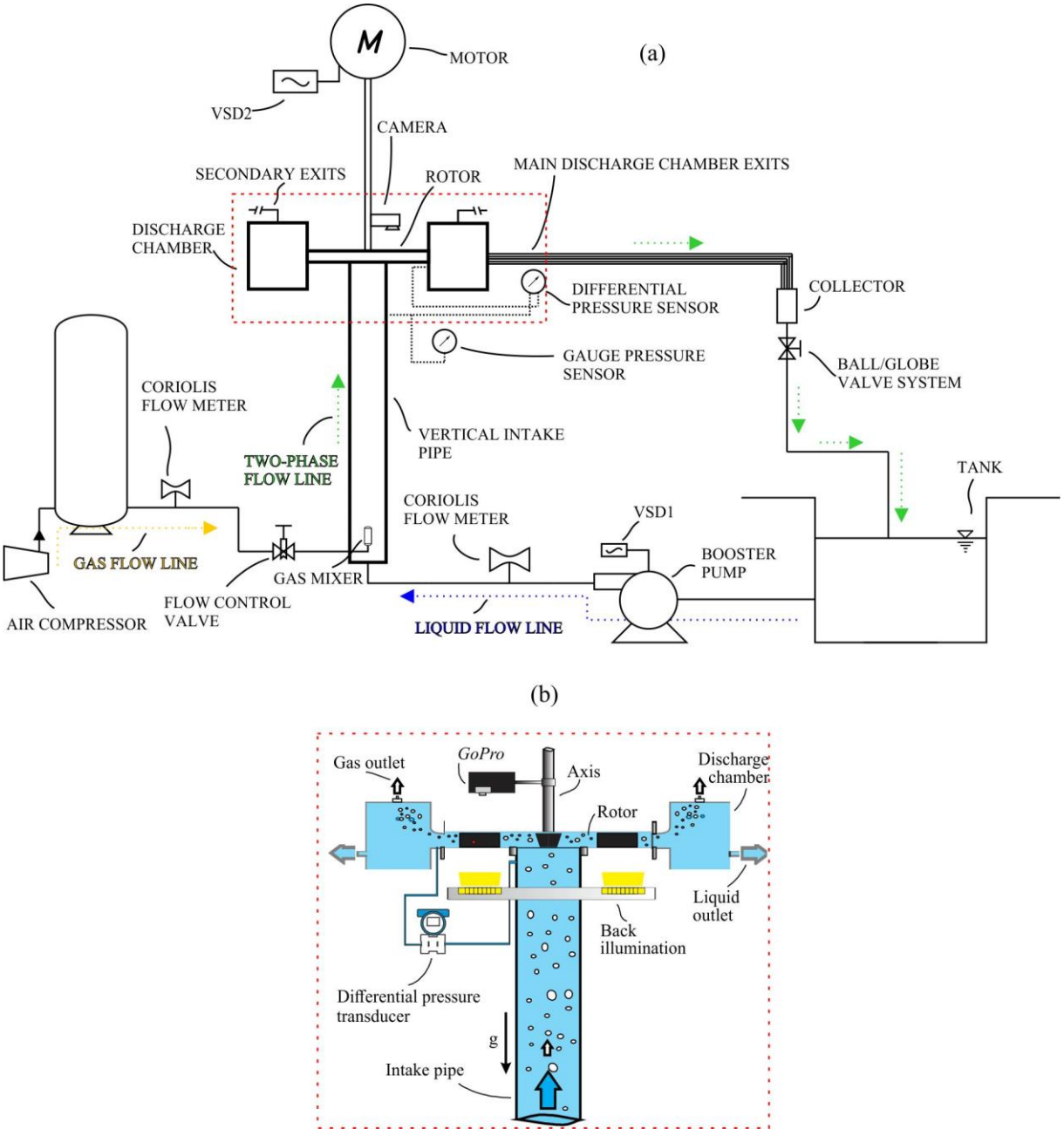

Figure 2. Scheme of the experimental loop (a) and the test section (b).

The rig is equipped with a differential pressure transducer to measure the pressure gain between the outlet and inlet sections of the rotor. A GoPro® camera is attached to the axis, allowing visualization in a rotating frame of reference, which greatly helps to analyze the relative motion of the gas phase inside the rotor channels. The rotor hub and shroud walls are flat, transparent and back-illuminated, which provides great definition for image processing. Results from this facility are useful to calibrate and validate the numerical model, by means of both performance data such as head versus flow rate curves at known gas flow rates, as well as valuable information obtained from the images, such as flow patterns and bubble size distributions. For single phase flow, the experiments were conducted varying the liquid flow rate from 0.5 to 15 m³/h, while the rotating speed varied from 200 to 500 rpm. For two-phase flow, the experiments were done for a single pressure rise curve at 300 rpm rotating speed and a gas mass flow rate equals to 0.06 kg/h.

4. RESULTS AND DISCUSSION

In this section, we present the results obtained in this work. Figure 3 presents the single phase curves expressed in a dimensionless form, where $\psi^p = (\Delta p/\rho_L)/(\omega \cdot D_{out})^2$ is the head coefficient based on the rotor static pressure rise (Δp)

and $\phi = Q_L / (\omega \cdot D_{out})^3$ is the flow coefficient, where $D_{out} = 2 \cdot R_{out} = 0.176$ m is the rotor outlet diameter, ρ_L is the liquid density and ω is the angular speed in rad/s. The curves show good agreement between them and confirms the affinity law of the rotor.

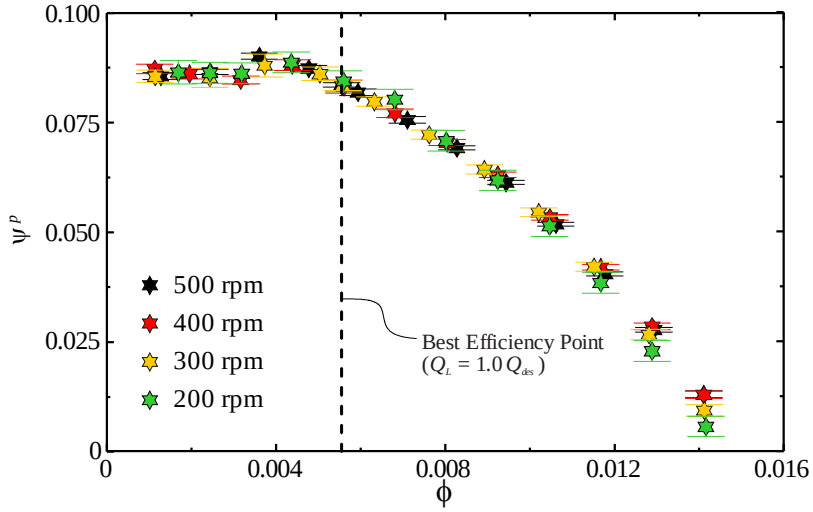

Figure 3. Head coefficient as function of the flow coefficient for different rotational speeds.

Figure 4 presents the experimental and numerical pressure rise curves for different rotational speeds. The numerical pressure rise is in good agreement with the experimental data for all rotational speeds and flow rates. Higher differences occurs for higher rotational speeds and flow rate above the BEP. Still, the coefficient of determination for all data series is $R^2 = 0.991$. In the Best Efficiency Point (BEP) the mean error between the numerical and experimental data is 3.6%.

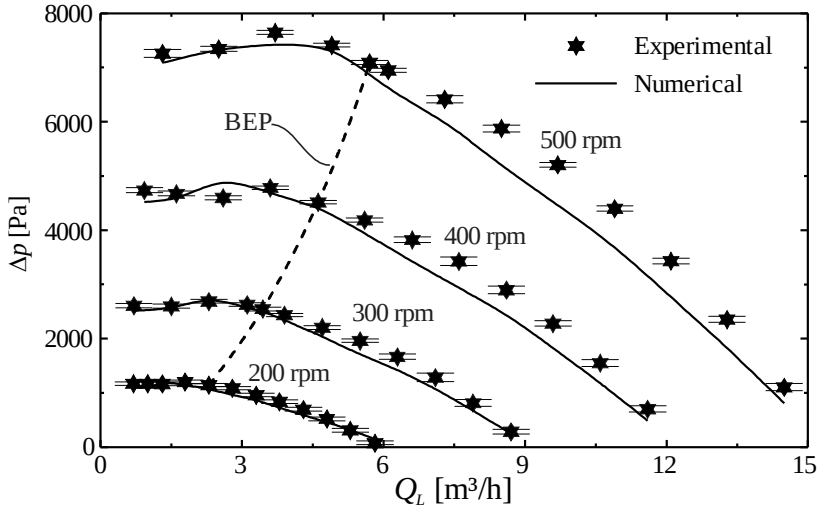

Figure 4. Experimental and numerical pressure rise curves, for single phase operation.

Figure 5 shows pressure gain versus liquid flow rate curves for single and two-phase flows. A nice agreement between numerical and experimental results is observed. One can notice that the model is able to capture the low degradation of the two-phase curve for high liquid flow rates compared to single-phase flow, and the abrupt performance drop around 4.7 m3/h as observed in the experiments, which is associated to the surging event. Such accordance depends on an adequate modeling of the main interface interactions and phase interaction such as breakup and coalescence.

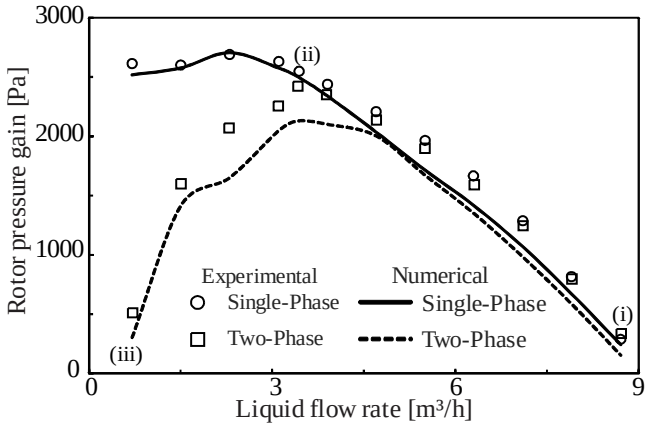

Figure 5. Pressure gain versus liquid flow rate curves for single and two-phase flows at a rotor speed of 300rpm.

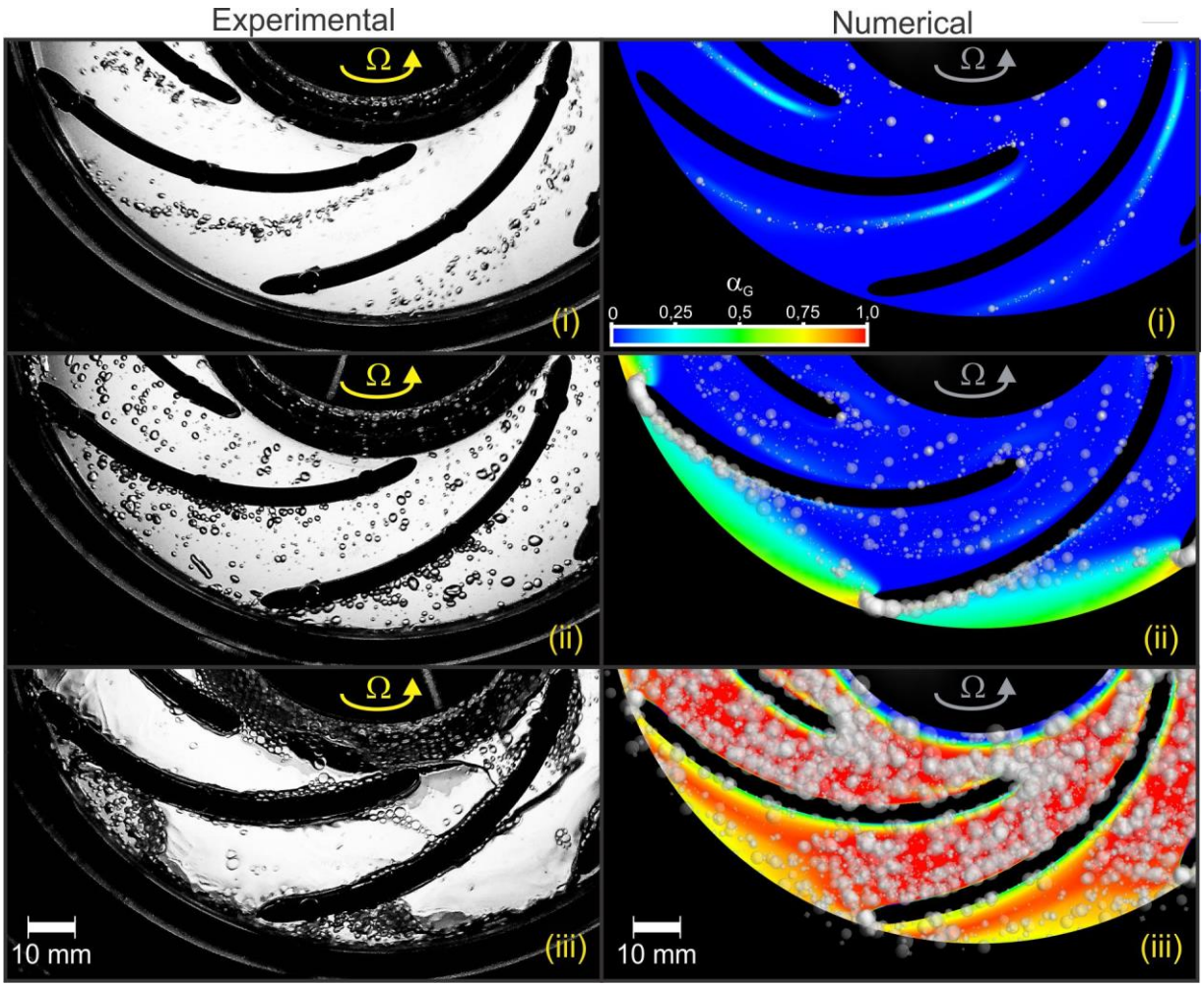

Figure 6. Experimental and numerical images of different flow patterns for 300rpm and m_g = 0.06 kg/h.

Figure 6 presents images of the flow pattern obtained experimentally and numerically for 300rpm and m_g = 0.06kg/h for liquid flow rates (i), (ii) and (iii) represented in Fig. 5. The bubbles in Fig. 6 (i) are dispersed and this condition is associated to lower pressure rise degradation as showed by Gamboa and Prado. (2012) and Monte Verde et al. (2017). Numerical result agrees well with the experiment. The trajectory of the bubbles are similar and the numerical model was able to capture different bubble sizes as is observed in the experiment.

In Fig. 6 (ii) the number of bubbles in the impeller channels increase. A preferable concentration of bubbles is seem near the blade pressure side and circumferentially near the exit, where coalescence of the bubbles occurs. The numerical model, again, was able to capture this trend. Although, for this case, the pressure rise degradation is higher in the

numerical data than the experiment. Still, surprisingly, the numerical model was able to capture the exact maximum pressure rise of the pump as in the experiment.

Figure 6 (iii) corresponds to the lowest inlet liquid flow rate. In this condition the gas phase occupies the whole channel of the impeller and causes a severe performance degradation. The numerical result shows bigger bubbles in the channel, which indicates the occurrence of bubble coalescence that may form gas pockets, which is in agreement with the experimental image. Furthermore, near the impeller exit, the bubbles are broken due to the shear in the wake of the gas pocket, which is in accordance, again, with the experimental image.

5. CONCLUSIONS

This work investigates gas-liquid flows in a centrifugal rotor assuming novel numerical and experimental techniques to overcome deficiencies from previous investigations. The numerical model includes a population balance model (MUSIG), which accounts breakup and coalescence of bubbles, besides several interfacial momentum transfer models. The experimental setup allows full visualization of one channel in a rotating reference frame, which facilitates the two-phase flow analysis as well as the image processing. The results from the numerical simulations has shown a good agreement with the experimental data. The single phase pressure rise curve is in good agreement with low deviation in the BEP flow rate. For two-phase flow, the numerical model was able to capture the pressure rise curve trend and even the maximum pressure rise was in the same liquid flow rate. Comparing the images obtained numerically and experimentally, one observes good agreement between them. Breakup and coalescence was captured in the numerical model in different conditions. In general, results from both approaches agree well and should help to bring further understanding on the complex gas-liquid flow patterns found in centrifugal pumps.

6. REFERENCES

Antal, S.P., Lahey, R.T. and Flaherty, J., 1991. “Analysis of Phase Distribution in Fully Developed Laminar Bubbly Two-Phase Flow”. *International Journal of Multiphase Flow*, v. 7, p. 635-652.

Caridad, J., Kenyery, F., 2004. “CFD Analysis of Electric Submersible Pumps (ESP) Handling Two-Phase Mixtures”. *Journal of Energy Resourcers Technology*, Vol. 126, p. 99-104.

Gamboa, J., 2008. *Prediction of the Transition in Two-Phase Performance of an Electrical Submersible Pump*. Ph.D. dissertation, The University of Tulsa, Tulsa, OK.

Gamboa, J. and Prado, M., 2012. “Experimental Study of Two-Phase Performance of an Electric-Submersible-Pump Stage”. *SPE Prodution and Facility*, 27(04), pp. 414-421.

Lo, S.M., 1996. “Application of Population Balance to CFD Modeling of Bubbly Flow via the MUSIG Model”. *AEA Technology*, AEAT-1096.

Luo, H. and Svendsen, H., 1996. “Theoretical Model for Drop and Bubble Breakup in Turbulent Dispersions”. *AIChE Journal*, v. 42, p. 1225-1233.

Monte Verde, W., Biazussi, L.J., Arrifano Sassim, N. and Bannwart C. A., 2017. “Experimental study of gas-liquid two-phase flow patterns within centrifugal pumps impellers”. *Experimental Thermal and Fluid Science*, 85, 37-51.

Murakami, M. and Minemura, K., 1974. “Effects of Entrained Air on the Performance of a Centrifugal Pump”: *1st Report, Performance and Flow Conditions. Bulletin of the JSME*, Vol. 17(110), pp. 1047 – 1055.

Prince, M.J. and Blanch, H.W., 1990. “Bubble Coalescence and Break-up in Air-Sparged Bubble Columns”. *AIChE Journal*, v. 36, p. 1485-1499.

Sato, Y. and Sekoguchi, K., 1975. “Liquid velocity distribution in two-phase bubble flow”. *International Journal of Multiphase Flow*, V. 2, P. 79–95.

Tomiyama, A., 1998. “A Struggle with Computational Bubble Dynamics”. *Third International Conference on Multphase Flow*. Lyon, France.

Yeoh, G.H. and Tu, J., 2009. *Computational Techniques for Multiphase Flows*, Butterworth-Heinemann, UK.

7. RESPONSIBILITY NOTICE

The authors are the only responsible for the printed material included in this paper.